Active optics system prototype applied on a passive large aperture off-axis LEO space telescope

Yang Sun
Kejun Wang
Wei Wang
Pingwei Zhou
Zhiyuan Gu
Jihong Dong
Shuyan Xu

Active optics system prototype applied on a passive large aperture off-axis LEO space telescope

Yang Sun,* Kejun Wang, Wei Wang, Pingwei Zhou, Zhiyuan Gu, Jihong Dong, and Shuyan Xu
China Academy of Sciences, Changchun Institute of Optics, Fine Mechanics and Physics, Changchun, China

Abstract. A large aperture space telescope with a passive structure with high stiffness and thermal stability can maintain a good image quality in a large span of disturbance. However, for the proposed more stringent requirements, it is beneficial to add active optics to the conventional design. In these telescopes, the off-axis design provides more design variables than the coaxis system and also provides greater adjusting ability for the active optics. We introduce an active optics system prototype deployed on an off-axis space telescope working at low Earth orbit. By adjusting the low-order aberrations of the primary mirror shape and adjusting the positions and attitudes of certain mirrors and the focal plane, the optical system's image quality corrupted by gravity discharge and temperature variation is increased to the undegraded level in the average sense in the full field of view. © 2018 Society of Photo-Optical Instrumentation Engineers (SPIE) [DOI: 10.1117/1.OE.57.11.115102]

Keywords: active optics; space telescopes; off-axis systems.

Paper 181201 received Aug. 18, 2018; accepted for publication Oct. 23, 2018; published online Nov. 19, 2018.

1 Introduction

A large aperture off-axis reflective optic system with aspheric or free-form surface shape provides a light, compact structure, more parameters for design, and good image quality and therefore is suitable for spaceborne astronomy observation. Such a space telescope consists of mirrors made of thermally stable materials with high stiffness, such as silicon carbide (SiC), and a solid support structure and can easily retain good image quality in a low Earth orbit (LEO) environment with an aperture of more than 1 m. However, when the aperture size is increased to more than 2 m and the enhancing optical indicator such as FOV calls for more rigorous design constraints, a completely passive structure could hardly maintain the optical system deformation within the range required for the desired image quality. In this case, active optics can be applied to the telescope. Different from the complex active optics system deployed on the James Webb Space Telescope, the LEO space telescope needs a design without a significant change to the original passive structure, despite the harsher thermal environment of LEO.

2 Overall Description of Active Optics System Prototype

2.1 Working Circumstances

Optical system structure misadjustments are caused by static and dynamic disturbances. Static disturbances include the long-term deformation induced by gravity discharge, thermal variation, temperature variation when going into and away from the Earth's shade, and stress release from the structure. Dynamic disturbances include the short-term vibrations induced by the solar array, reaction wheel, and liquid fuel flow motion. In this work, only misadjustments caused by the static disturbances are handled by the LEO space telescope's active optics system. The influence from the external and on-board dynamic disturbances is handled by the image

stabilization system on the space telescope, as are the vibrations induced by the active optics system adjustment. A continuous adjustment similar to that in adaptive optics is not required because effects such as atmospheric disturbance are absent in the orbital environment. Instead, periodic intermittent adjustment is appropriate.
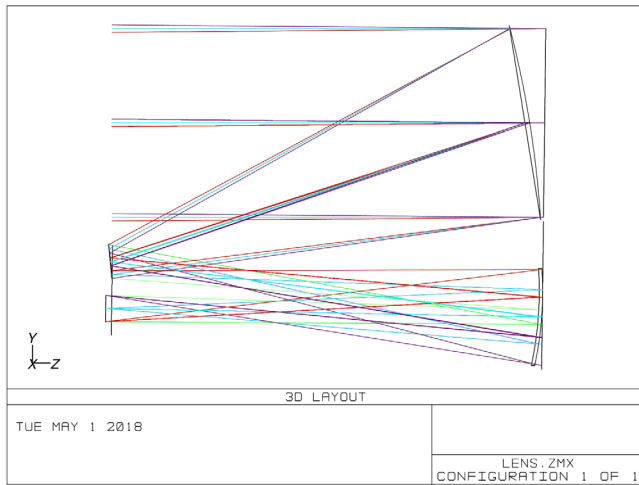
2.2 Optical System

In this article, we demonstrate the active adjustment and analyze the active optics system prototype (AOSP) performance based on a typical passive three-mirror off-axis system shown in Fig. 1. The parameters of the optical system are listed in Table 1. The AOSP's optical aperture is 73% of the aperture of WFIRST, and the FOV of AOSP is set to 1 deg × 1 deg. Such an optical system in practical tasks is always followed with a harsh environmental sensitivity. The primary mirror (PM) has an aspherical surface shape with a conic constant of −0.91. All of the mirrors are made of SiC for high stiffness.

2.3 Working Process of AOSP

To provide a feedback index for evaluating whether the optical system imaging performance is enhanced to the undegraded level, AOSP employs C_{OS} as the total criterion of the system image quality. C_{OS} integrates one or several image quality indicators, such as the wavefront error (WFE), Strehl ratio, or ellipticity, collected from the entire FOV and is a statistical value calculated from multiple FOV positions that collects the weighted effects described by the image quality indices. In this article, C_{OS} is the average value of the aberrations sampled at different FOV points. The description of the practical implementation is provided below in the discussion of the listed AOSP modules.

The AOSP includes three parts: the measurement module, solution module, and execution module. The measurement module measures the image quality indicators using the

---

Fig. 1 Optical system design.

Table 1 Parameters of the telescope optical system on which the AOSP is deployed.

Parameter	Value
System aperture	1.75 m
System focal length	14 m
FOV	1 deg × 1 deg square
WFE	0.0310λ
Wavelength	0.6328 μm

wavefront sensors on the focal plane (FP) and the main astronomical CCD array of the optical system. The solution module is a set of algorithms that receives the image quantity values from measurement module and calculates the values of the adjustment parameters for the execution module. The execution module executes the adjustment orders from the solution module with a series of mechanisms, namely, the PM active support system with actuators at the PM backside used to adjust the shape, a Stewart platform supporting the second mirror (SM) with adjusted positions and attitudes, and the conventional FP focusing mechanisms.

When C_{OS} is found to be below the specified level of similarity to the undeformed extent during regular monitoring from the measurement module, the solution module solves for the adjustment parameters, and then the telescope optical system is adjusted by the execution module. After a round of adjustments, the telescope image quality is measured again. If the adjusted C_{OS} is still unsatisfactory, the active optics loop is executed again until the image quality converges to the desired level.

Since the AOSP operates in the transition stage from a passive optical system to an active system, an optical margin must still be allocated conservatively to account for image quality degradation from gravity discharging and thermal variation, even though such degradation will be recovered by active optics in a pure active telescope. The image quality margin range between the optical design level and the modularized optical system level is the space utilized by the AOSP. On the one hand, the adjustment always transforms the optical system to a new shape that may lead to the image quality decreasing slightly from that of the original optical design; active measuring and solving and executing errors from the AOSP also lower the image quality. On the other hand, the AOSP suppresses the image quality degradation from the gravity discharge and thermal effects that are still included in the optical margin of the conventional passive design. When the enhancement effect from the AOSP exceeds the degradation effect, the overall image quality is enhanced to the nearly undegraded level.

The image quality of an optical system can be described by many indicators such as WFE, Strehl ratio, and encircled energy. C_{OS} should include the indicators measured at several representative points on the FP to describe the overall FOV performance. The AOSP takes the Zernike-term-formed WFE from several FOVs as the output from the measurement module and the input to the solution module to calculate the adjustment parameters. In the execution module, PM shape adjustment parameters generated by the solution module are also expressed as the Zernike terms that are transformed to the forces applied by specific actuators to the PM. In the solution module, C_{OS} includes several kinds of indicators, whereas in the active optics adjusting simulation described in this article, only the WFE is adopted as C_{OS}.

During the telescope's routine work, adjustments are made every 2 h to eliminate the effect from thermal impact caused by the telescope's entering and exiting the shadow of earth. The telescope does not have to change its attitude in such adjustment. Precise adjustment is performed once a week, during which the telescope is pointed deliberately at the direction near the galactic center with higher density of the bright stars to ensure a higher accuracy of WFS. Each calibration included five to six iterations, all of which were completed within about 10 minutes, considering the heat dissipation efficiency of the PM adjusting mechanism.

3 Measuring Module

3.1 Introduction

The measurement module supplies image quality indicators that comprise the C_{OS} used for evaluating the optical system performance. Although the use of additional indicators can provide a more specific active strategy for the telescope's astronomy task, the AOSP only takes the WFE to support solving and adjustment. Measurements should be carried out at multiple different FOV locations to collect the optical structure information.

The AOSP takes the main astronomical CCD and a suit of wavefront sensors attached on the edge of the main astronomical CCD as two independent methods for measuring the WFE values. Wavefront sensors have the advantage of frequent measurements that do not affect the main astronomical observation task, whereas measurements with the main CCD array will take a fraction of the observation time and may lead to focusing error. A whole measurement with the main CCD array includes one focus adjustment and two exposures and therefore may take longer than the measurements with the wavefront sensor. The disadvantage of the wavefront sensor is the weaker image quality describing

the performance at fewer measured FOV positions than for the measurements with the main CCD array, making the image quality and optical system structure information more sparse and localized.

3.2 Wavefront Sensor Construction

Wavefront sensors are set up at the centers on the four edges of the main imaging region, corresponding to (−0.5 deg, 0 deg), (0.5 deg, 0 deg), (0 deg, −0.5 deg), (0 deg, 0.5 deg) on the FOV. Each wavefront sensor has a beam splitter with its two sides attaching two CMOS patches. One is attached on the focal position, and the other is attached on the defocus position. The incident light is divided into two beams by the beam splitter and focused on the two CMOS patches to give images for WFE solving. Each sensor takes up a tiny area of the optical system FP and provides WFE at the FOV of the sensor's position (Figs. 2 and 3).

Wavefront sensors can work independently of the astronomical observation task and can reach a high measuring frequency to achieve a fast correction iteration. Therefore, wavefront sensors are used as the main measuring device of active adjustment. Wavefront sensors and their distribution at the edge of the main astronomical CCD array, measurement using wavefront sensors alone sometimes cannot iterate to the optimum image quality level due to the lack of wavefront aberration from comprehensive FOV. In addition, in the regular evaluation of the optical system image quality, the aberration information from the FOV of the main CCD array is also needed. Therefore, it is also necessary to make the main CCD array capable of wavefront sensing. For this purpose, the main CCD array needs to provide on-focus and defocus images of the same star point. Such measurements are less than sensing only using wavefront sensors, in order to reduce the risk of optical system image quality degradation.

The main CCD array provides small image fragments containing star PSFs on the previously assigned FOV situations for wavefront sensing. Defocus images from the main CCD are obtained by tuning the optical focal length by a specified distance (Figs. 2 and 3).
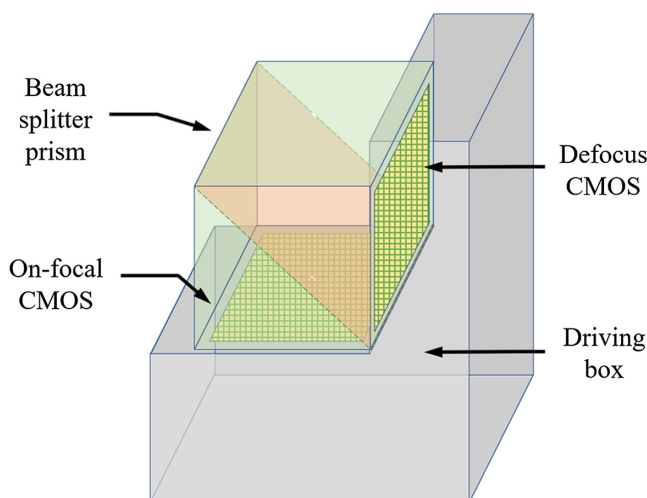
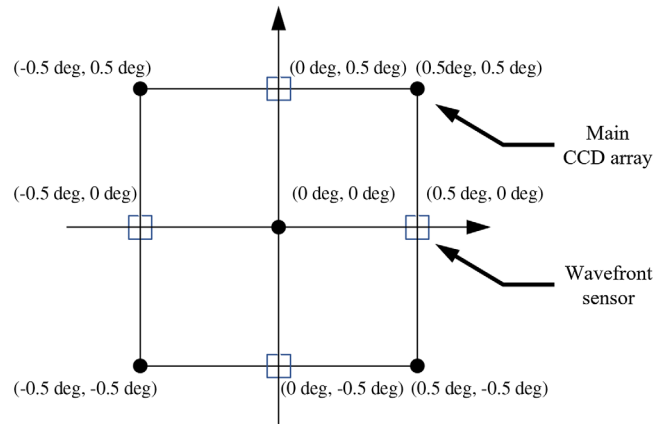

Fig. 2 Illustration of a wavefront sensor.

Fig. 3 Wavefront sensors and the main astronomical CCD array sampling locations on the FP.

3.3 Measurement Algorithms

The wavefront sensing techniques considered for space astronomical observation include the Shack–Hartmann sensor, pyramid prism sensor, phase diversity (PD), and phase recovery algorithm.[1–7] The measurement module uses PD as the main method in wavefront sensing because it is not necessary to separate the optical path and better convergence efficiency.

The PD algorithm provides 4th to 11th Zernike terms of the aberration at each FOV measuring point. The first three terms cannot be obtained using the PD algorithm. As low-order aberrations, the 4th to 11th terms are always larger than the higher order aberrations, which is suitable for solving for the adjustment parameters.

C_{OS} is given as

$$C_{\mathrm{OS}} = \frac{\sum_{i=1}^{4} \mathrm{WFE}_{i,1} + \sum_{j=1}^{5} \mathrm{WFE}_{j,2}}{9}, \qquad (1)$$

where $\mathrm{WFE}_{i,1}$ is measured by the i'th wavefront sensor, and $\mathrm{WFE}_{j,2}$ is measured by the j'th FOV point on the main CCD array. $\mathrm{WFE}_{i,j;1,2}$ is the sum of the 1st to 37th Zernike terms at each FOV given as

$$\mathrm{WFE} = \sum_{k=1}^{37} a_k Z_k, \qquad (2)$$

where Z_k is the fringe Zernike term, and a_k is the coefficient. In the parameter adjustment, the working used WFE data are solved only using the data from the four sensors, and no WFE data are collected from the main CCD array to prevent unnecessary FP drift in defocus image acquisition.

4 Solving Module

4.1 Introduction

The solution module calculates the parameters of the adjustment to be applied for the optical system structure from the image quality information supplied by the measurement module. The input data of the solution module consist of the optical system indicators given by the measurement module, that is, C_{OS} and the 4th to 11th Zernike terms of WFE. The output data of the solution module consist of the 4th to

11th Zernike terms of the PM surface shape error and the adjustments of the position and attitude on the SM and FP.

The 4th to 11th Zernike terms are the dominant deformations that often appear on the PM shape and can be easily produced by PM active supports. Taking the PM as a stationary reference to the optical system, the first to third Zernike terms are converted to other mirrors' misadjustment amounts and therefore can be discarded. As higher-order WFEs, the terms of the order higher than 11 are also neglected because the effects of these terms are often submerged by noise and can make the problem overconstrained.

The SM adjustment parameters involve three-direction translation and the x/y tilt. The discarded last degree of freedom, namely, rotation across the optical axis, leads to the image degradation magnitude that is two orders of magnitude smaller than the other degrees of freedom for similar deformation extents, even if an off-axis or aspherical/freeform surface design is adopted.

FP adjustment parameters involve piston and x/y tilt that inherit the focusing feature in the intrinsic design of the passive optical system and are responsible for compensating the tilt of the FP.

No adjustment parameters are used on the third mirror (TM) because the complexity due to adding the adjusting mechanisms on TM exceeds the benefits of adjusting.

4.2 Solving Algorithms

The relationship between the image quality indicators and adjustment parameters can be approximated with a sensitivity matrix model in the linear and quadratic orders. In addition to the WFE, other types of indicators can be incorporated into the two models. If the scope of the image quality indicators is limited to the WFE, a more precise description of the optical system structure can be given based on the nodal aberration theory.

4.2.1 Linear and quadric sensitivity matrix model

Every adjustment parameter affects all of the image quality indicators at each FOV position in different distributions. The image quality indicators are given as

$$W = [w_1, w_2, \cdots, w_k]^T, \qquad k = m \times n, \qquad (3)$$

where $w_i(i = 1, \cdots, k)$ are the image quality indicators such as a Zernike term, Strehl ratio, or encircled energy; m is the FOV position where the indicators are measured; and n is the number of indicators at each position. In the AOSP, $k = 32$ with $m = 4$ is the amount of the wavefront sensors, and $n = 8$ because 4th- to 11th-order Zernike terms are used. The adjustment parameters are listed as a column vector

$$X = [x_1, x_2, \cdots, x_l]^T, \qquad (4)$$

where $x_i(i = 1, \cdots, l)$ are the adjustment parameters such as the WFE Zernike term of the PM shape and the degree of freedom of SM or FP for adjusting. In the AOSP, $l = 16$ includes the eight Zernike terms of the PM shape, five degrees of freedom of SM, and three degrees of freedom of FP. If the PM shape adjustment is not performed, $l = 8$.

The relationship between W and X can be expanded to the first order as

$$W_r^L = W_0 + \mathbf{M}_1 X, \qquad (5)$$

and to the second order as

$$W_r^Q = W_0 + \mathbf{M}_1 X + \frac{1}{2}\mathbf{M}_2 X^2, \qquad (6)$$

where W_0 is the image quality indicator value column of the original undeformed system, W_r is the indicator value column of the deformed system calculated to linear and quadratic orders, and $\mathbf{M}_1$ and $\mathbf{M}_2$ are the linear and quadratic sensitivity matrices under the first- and second-order approximations. In a small region around the undeformed state of the optical system, the higher-order residuals can be ignored.

In the AOSP, W_0 is chosen at the undeformed state with $C_{OS} = 0.03\lambda$ according to Eq. (1). The i-'th column m_{1i} in $\mathbf{M}_1$ is given as

$$m_{1i} = \frac{W_{ri} - W_0}{\Delta x_i}, \qquad i \text{ from 1 to } k, \qquad (7)$$

where W_{ri} is the image quality indicator value column with only the i-'th misadjustment value Δx_i affecting the optical system. Δx_i value is selected to make C_{OS} degrade by 0.3λ.

The i-'th column m_{2i} in $\mathbf{M}_2$ is given as

$$m_{2i} = \frac{W_{rpq} - W_{rp0} - W_{r0q} + W_0}{\Delta x_p \Delta x_q}, \qquad p, q \text{ from 1 to } k, \qquad (8)$$

where W_{rpq}, W_{rp0}, and W_{r0q} are the image quality indicator value columns under the simultaneous Δx_p and Δx_q actions, only under Δx_p, and only under Δx_q, respectively. $\mathbf{M}_1$ and $\mathbf{M}_2$ will be calibrated in the testbed stage. Several groups of sensitivity matrices taken from different misadjustment ranges should be prepared to fit different deforming severity levels or different stages in the iterative adjustment.

X^2 is written in the column vector form as

$$X^2 = [x_1^2, x_1 x_2, x_1 x_3, \cdots, x_l^2]^T, \qquad (9)$$

where every element is a product of two indicator values. For this form of X^2, Eq. (6) transforms into a problem with k equations and $l(l+1)/2$ variables. Similar to the linear form given in Eq. (5), $x_i x_j$ are solved together with x_i as additional variables, and then Eq. (6) can be easily solved using algorithms such as regression analysis and singular value decomposition (SVD).

The measurement module should supply enough image quality indicators to ensure that the problem is solvable, that is,

$$k \geq \begin{cases} l, & \text{under linear approximation} \\ l(l+1)/2, & \text{under quadratic approximation} \end{cases}. \qquad (10)$$

This demand can be satisfied by taking enough FOV points to measure the image quality and select enough indicators. A greater number of indicators can provide a better solution with an appropriate algorithm, and larger indicator values are desired to restrain illconditioning and noise.

4.2.2 Nodal aberration theory

Axial symmetry is broken down with the off-axis design applied on the optical system, and therefore, the aberration distribution throughout the FOV becomes rotationally asymmetric. Wave aberration caused by misadjustment proceeds across the posterior surfaces along the light transmitting direction and is expressed differently in connection with the FOV. The relationship between the wave aberration distribution and misadjustments can be described by the nodal aberration theory. Using several WFE samples measured from the different FOV, the optical structure parameters can be obtained, and misalignments can be acquired.[8–11]

When misadjustment is caused by or manifests as mainly as lower-order WFE terms but is compensated by the higher-order terms, the optical system shape after the adjustment may transform to an illconditioned state: the subsequent deformed situation will be more complex and strange, and the next adjustment will be more difficult. The adjustment units are employed conservatively in the AOSP; that is, the order of preference for the adjustment of the optical system is only with the FP, then with both the SM and FP, and then with the PM, SM, and FP. This strategy is particularly suitable for the nodal aberration algorithm that forecasts the optical system state before the adjustment is selected. With this method, the stability of the optical system shape during multiple adjustments will be enhanced.

5 Executing Module

The execution module includes the active support mechanism on the PM, a Stewart platform that supports the SM, and the adjusting mechanism for the FP.
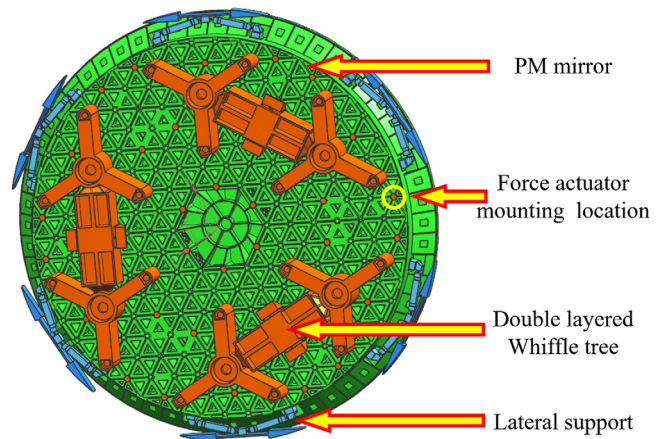
5.1 PM Active Support Mechanism

The PM active support mechanism involves a high stiffness back plate mounted in the mirror cell, three branched whiffle trees attaching the mirror at the backside to the back plate to provide a passive way to support the PM, three lateral support structure constraining the remaining degrees of freedom of the PM, and 36 force actuators deployed at the back of the PM that are responsible for the surface shape adjustment, as shown in Fig. 4.

Under the gravity environment, the weight of the PM is sustained by the three-point passive support. The three-point passive support design involves two whiffle tree layers. In the first layer, each support point on mirror cell has two branches. In the second layer, each branch links the PM backside by Y-shape distributed three points. With this design, PM can maintain the position without interfering the actuators adjusting the mirror shape on orbit. The actuators are arranged in three concentric circles at the back of PM and in 120 deg symmetry matching with the passive support. The actuators will not be unlocked until the telescope is launched into orbit.

5.2 Converting the PM Figure to the Actuator Force

By applying push or pull forces onto the PM backside, the WFE can be added to the shape to execute the PM adjustment. The amplitudes of the WFE produced on the PM shape are linearly proportional to the actuator forces. The solution module provides the WFE to be added on the PM that are converted to the actuator forces using the sensitivity matrix

Fig. 4 The PM active support mechanism. The double Y-shape pairs are passive branched whiffle trees. The darker dots on the intersections of PM's beams are the positions of the deployed actuators. The Whiffle tree's design needs optimization to reserve space for nearby actuators. Six groups of lateral support structures are placed near the edge of PM. The mirror cell is not shown.

method as introduced in the solution module. The exact actuator positions adopted on the PM are optimized using the Monte Carlo method to generate accurate Zernike terms (Fig. 5).

The adjusting forces exerted by the actuators are optimized using an SVD algorithm. The eigenmodes are extracted from the sensitivity matrix of the PM figure and represent the mechanical characteristics of the PM module. The deformed figure can be expressed as a sum of these modes (Fig. 5). A higher vibration frequency corresponds to a higher figure mode that is produced by larger forces and has a smaller effect on the wavefront. The actuator forces are significantly reduced in adjusting by filtering away the high-order modes.

The SM adjusting mechanism uses the Stewart platform to adjust five SM degrees of freedom. In the testbed stage, due to gravity, the travel distance along the vertical direction in the aligning process is preserved to ensure that SM moves back to a good position of the Stewart platform after a gravity discharge.

The FP adjusting mechanism adds a piezoelectric driven x/y-tilt platform to the focusing mechanism design to enable the FP to cooperate with other adjusting mechanisms. If a folding mirror is inserted before the FP to make the entire optical system more compact, the FP adjusting mechanism can be mounted on the folding mirror module.

6 Active Adjusting Simulation

Adjusting performances under different conditions are compared in several groups using the Monte-Carlo method. Each group involves 100 independent experiments in which uniformly and randomly generated misadjustment values are assigned to the adjustment parameters. Each misadjustment value does not exceed degrading C_{OS} by $\pm 1\lambda$ or $\pm 0.3\lambda$ when added alone to the optical system. The misadjustment values are added immediately before the active optics are initiated. No more deformation is added thereafter in the adjustment loops. The adjustment iterates until C_{OS} reaches 0.035λ, or the number of iterations reaches 5.
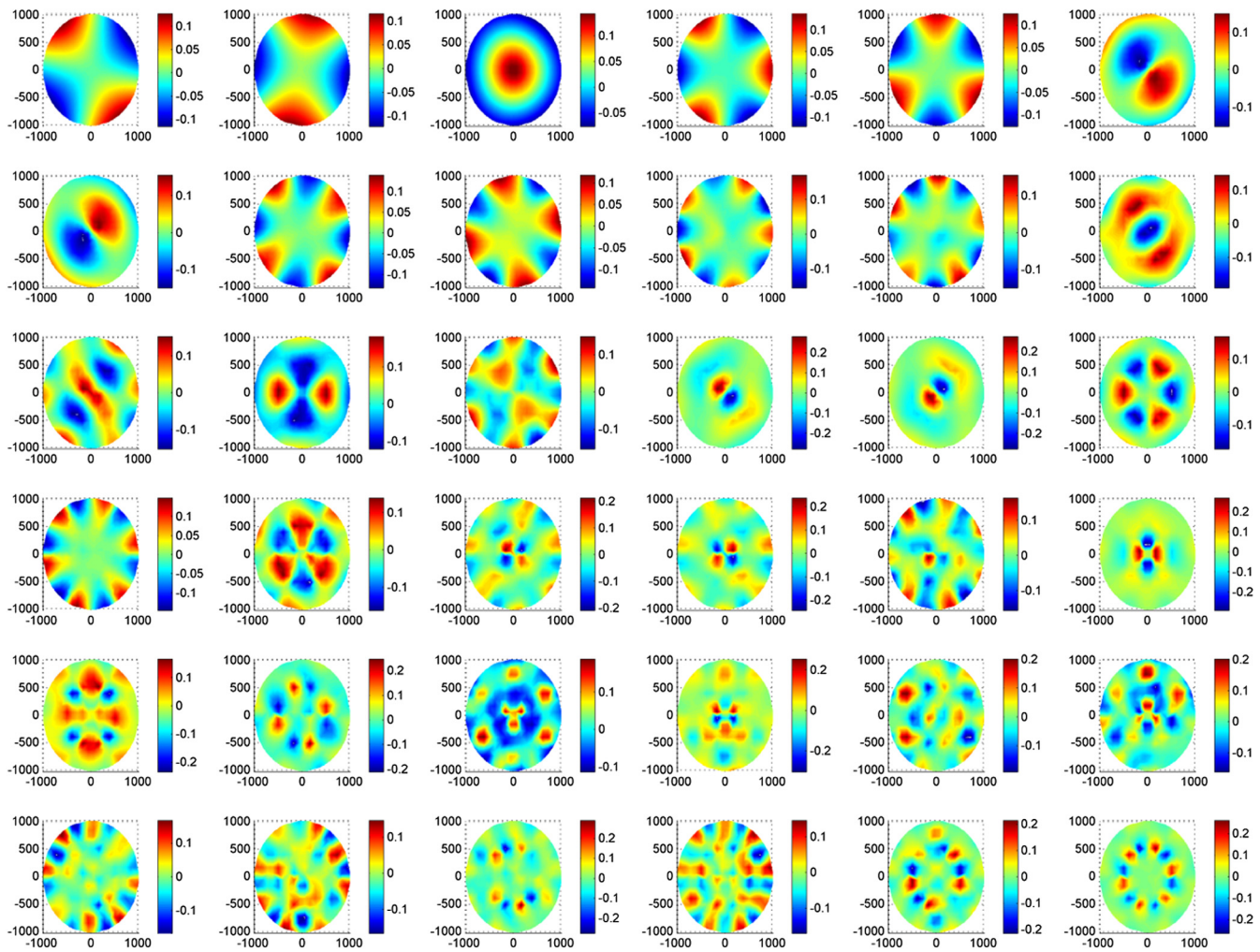
Fig. 5 Eigenmodes of the PM FEA model. XY coordinates are in mm. The bars describe the PV value of each PM figure in λ.
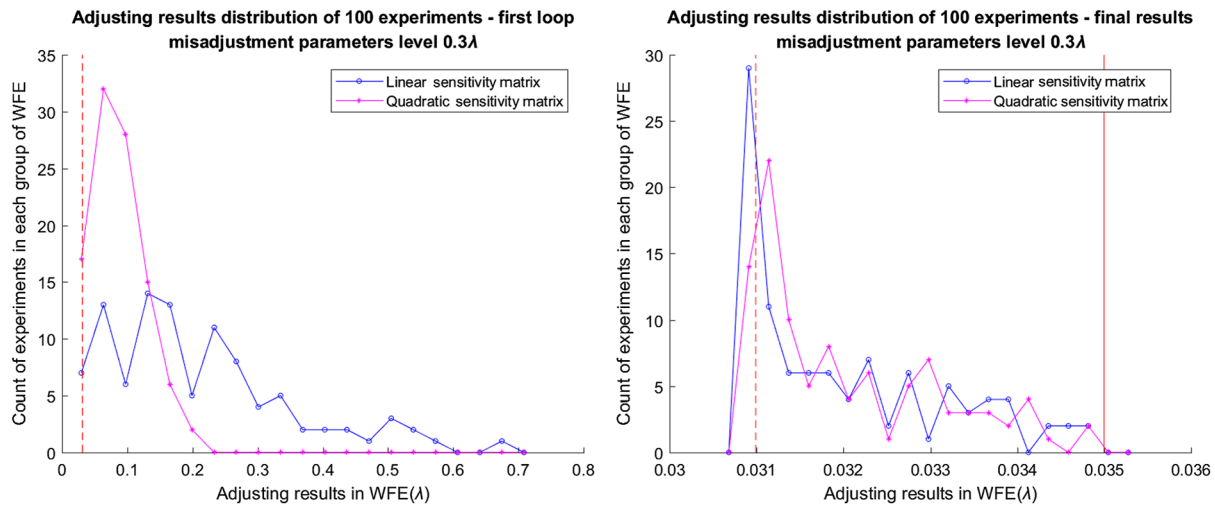

(a) (b) (c)
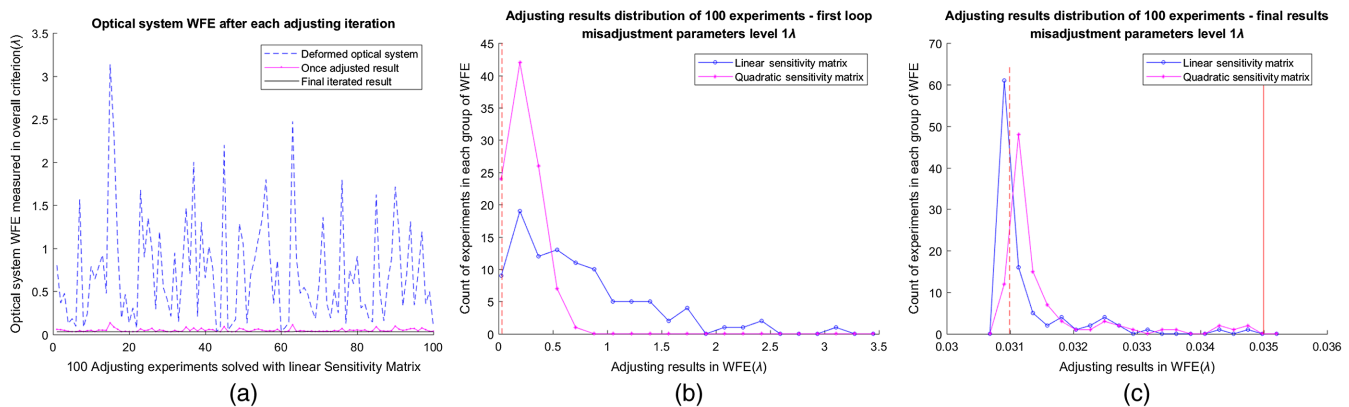
Fig. 6 Adjusted results of 100 experiments. Each misadjustment random value is uniformly selected between $\pm 1\lambda$.

Figure 6(a) shows the deformed and adjusted C_{OS} solved with the linear sensitivity matrix algorithm. The blue dashed line represents the randomly assigned deformed optical system WFE that makes C_{OS} increase to the 1λ level from 0.03λ of the initial undeformed system. The magenta-dotted line shows that after the first adjustment loop, in most

experiments, C_{OS} decreases rapidly to below 0.035λ, which means that the optical system is successfully adjusted. The black solid line is below 0.035λ, which means that all deformed systems are adjusted. Figure 6(b) compares the operational efficiencies of the linear and quadratic algorithms. Each point in the plot represents a count of the

Fig. 7 The adjusted results of 100 experiments. Each misadjustment random value is uniformly selected between ±0.3λ.

experiments with C_{OS} falling around the point's WFE value. After the first loop, C_{OS} along the testing group with the quadratic algorithm focused more toward the undeformed system state than for the group with the linear algorithm. Figure 6(c) shows the final adjusted results obtained by the two algorithms. The vertical dashed and solid lines in Fig. 6(c) indicate 0.03λ and 0.035λ, which respectively are the initial undeformed optical system image quality and the adjustment goal. The distribution of the two groups of the adjusted results presented in Figs. 6(b) and 6(c) shows that the quadratic model provides a better description up to 1λ level as C_{OS} is degraded, whereas in a small range in the vicinity of the initial state, the linear model performs better.

Figure 7 shows the first and final adjustment iteration results with the optical system deformation extent decrease to 0.3λ. The shape and tendency of C_{OS} distribution are still unchanged, and the final adjusted results are distributed more widely than in Fig. 6.

Figure 8 compares the adjusted results obtained using the adjustment parameters including and excluding the PM active support mechanism, where equal misadjustments of

the PM shape are added in both situations. Adjusting without the PM parameters shows a higher convergence rate benefiting from a more concise and less illconditioned sensitivity matrix, whereas the final iteration gives much more dispersed final C_{OS} in a wide range, and half of the experiments fail to converge at the 0.035λ target. This shows that without the PM shape adjusting ability, the AOSP could still compensate the PM shape deformation influence by adjusting the degrees of freedom of other mirror in a limited range, and in this way, the adjusting effect would be reduced.

Figure 9 compares the adjusted results with errors uniformly and randomly assigned in the scope of ±5% from the execution module and 0.5% from the measurement module. The sensitivity matrix algorithm behaves more sensitive to measurements than adjustments. Considering it is not easy to enhance the accuracy in our wavefront sensing algorithms, reducing sensitivity matrix morbidity is essential. On the other hand, the fact that the adjusted results are insensitive to errors of adjusting movements means that larger execution errors are tolerable, and adjusting PM figure with sensitivity matrix method as an open-loop procedure is feasible.
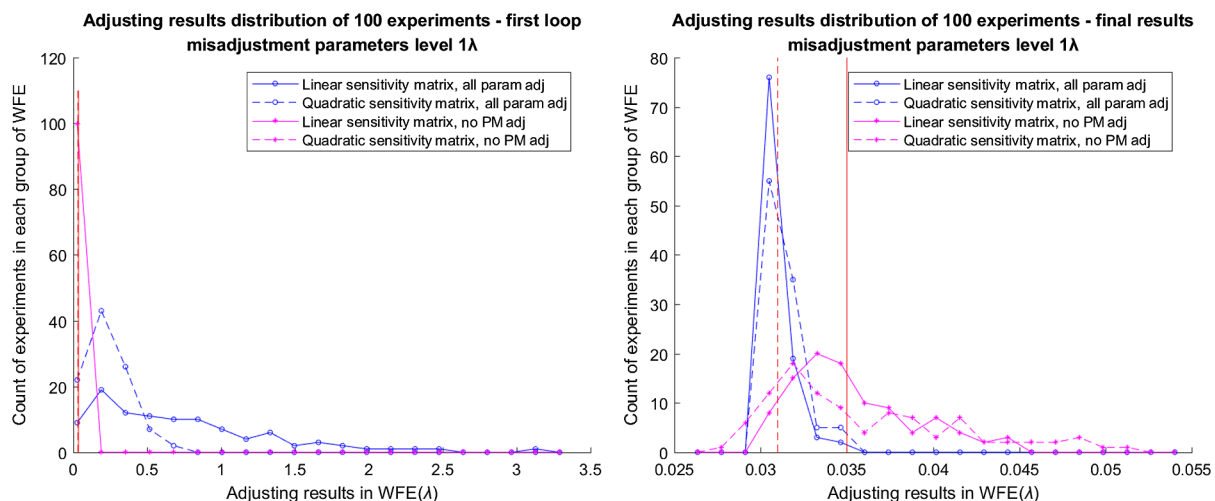
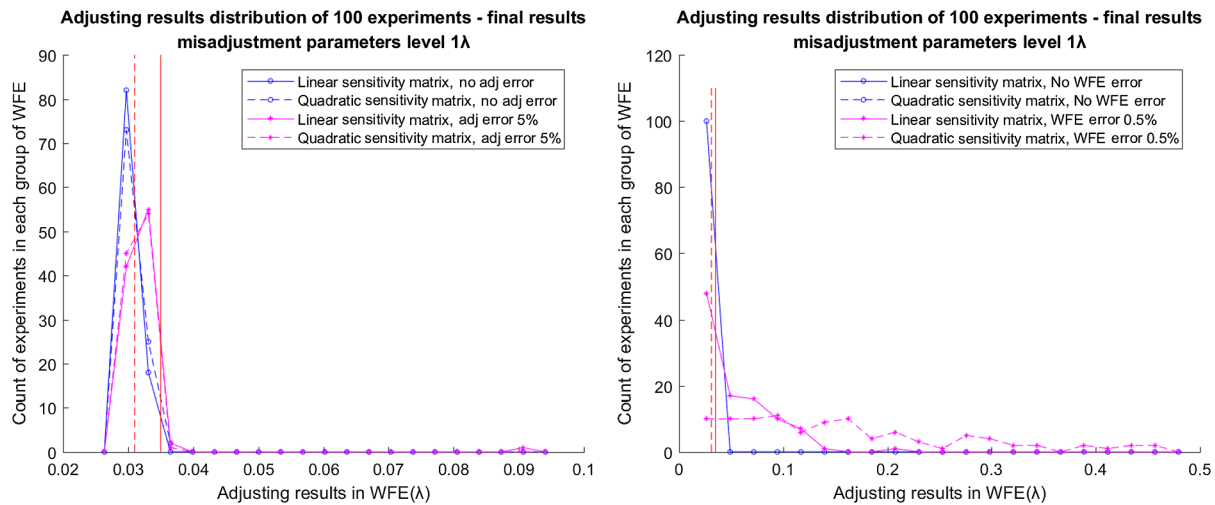**Fig. 8** The adjusted results with different ranges of adjustment and misadjustment parameters.

Fig. 9 Adjusted results with measuring and executing errors.

7 Conclusion

We have designed an active optics system prototype for passive large off-axis space telescope construction. Through adding the prototype on an optical system consisting of SiC mirrors, active adjusting ability is obtained without too much modification to the primary telescope design. The adjustment simulation shows that the prototype has the potential to restore the optical system imaging quality from 1λ caused by environmental factors to near the undegraded level 0.035λ after iteration no more than five times. This allows the space telescope to employ a 2-m level monolithic SiC PM and a more environmentally sensitive optical design and does not need to increase the manufacture cost too high.

Acknowledgments

References

1. J. S. Knight et al., "Hartmann test for the James Webb space telescope," *Proc. SPIE* **9904**, 99040C (2016).
2. S. Esposito et al., "Pyramid wavefront sensor at the William Herschel telescope: towards extremely large telescopes," *ING Newsletter* (10), 17–18 (2005).
3. R. A. Gonsalves, "Phase retrieval and diversity in adaptive optics," *Opt. Eng.* **21**, 829–832 (1982).
4. J. R. Fienup, "Phase retrieval algorithms: a comparison," *Appl. Opt.* **21**(15), 2758–2769 (1982).
5. J. S. Smit et al., "Phase retrieval on broadband and under-sampled images for the JWST testbed telescope," *Proc. SPIE* **7436**, 74360D (2009).
6. C. S. Smith, R. Marinica, and M. Verhaegen, "Real-time wavefront reconstruction from intensity measurements," in *3rd AO4ELT Conf.: Adaptive Optics for Extremely Large Telescopes* (2013).
7. C. S. Smit et al. "Iterative linear focal-plane wavefront correction," *J. Opt. Soc. Am. A* **30**(10), 2002–2011 (2013).
8. J. Sasián, "Theory of sixth-order wave aberrations," *Appl. Opt.* **49**(16), D69–D95 (2010).
9. K. P. Thompson, T. Schmid, and J. P. Rolland, "The misalignment induced aberrations of TMA telescopes," *Opt. Express* **16**(25), 20345–20353 (2008).
10. K. P. Thompson, "Multinodal fifth-order optical aberrations of optical systems without rotational symmetry: the astigmatic aberrations," *J. Opt. Soc. Am. A* **28**(5), 821–836 (2011).
11. T. Schmid, "Misalignment induced nodal aberration fields and their use in the alignment of astronomical telescopes," PhD Dissertation, University of Central Florida, Orlando, Florida (2010).

Yang Sun is an assistant researcher at Changchun Institute of Optics, Fine Mechanics and Physics (CIOMP), China Academy of Sciences. He received his BS degree in physics from the University of Science and Technology of China in 2008. He received his PhD in optics from CIOMP in 2013. His current research interests include space active optics, space telescope technology incorporates with fiber optics, computational optics, image processing technology, etc.

Pingwei Zhou received his BS and MS degrees in mechanical engineering from Northwestern Polytechnical University in 2011 and 2014, respectively. Currently, he is working toward his PhD at Changchun Institute of Optics, Fine Mechanics and Physics, Chinese Academy of Sciences. His research interests include lightweight mirror design and space active optics.

Zhiyuan Gu is a research assistant at Changchun Institute of Optics, Fine Mechanics and Physics, Chinese Academy of Science. He received his BS and PhD degrees in optical engineering from Dalian University of Technology in 2009 and from the University of Chinese Academy of Sciences in 2016, respectively. His research interests include active optical correction algorithms for large aperture telescope, optical system alignment, and unconventional optical system design.

Biographies for the other authors are not available.